Pharmacokinetic modeling of the Second-wave Phenomenon in Nanobubble-based Contrast-enhanced Ultrasound

Document license:
TAVERNE

DOI:
10.1109/TBME.2022.3184266

Document status and date:
Published: 01/01/2023

Document Version:
Publisher's PDF, also known as Version of Record (includes final page, issue and volume numbers)

Please check the document version of this publication:

• A submitted manuscript is the version of the article upon submission and before peer-review. There can be important differences between the submitted version and the official published version of record. People interested in the research are advised to contact the author for the final version of the publication, or visit the DOI to the publisher's website.
• The final author version and the galley proof are versions of the publication after peer review.
• The final published version features the final layout of the paper including the volume, issue and page numbers.

Link to publication

Pharmacokinetic Modeling of the Second-Wave Phenomenon in Nanobubble-Based Contrast-Enhanced Ultrasound

Chuan Chen , Reshani Perera, Michael C. Kolios , *Senior Member, IEEE*, Hessel Wijkstra, Agata A. Exner , Massimo Mischi , *Senior Member, IEEE*, and Simona Turco , *Member, IEEE*

Abstract—**With a typical 100–500 nm diameter, nanobubbles are a promising new-generation ultrasound contrast agent that paves ways for several applications, such as efficient drug delivery, molecular imaging, and assessment of vascular permeability. Due to their unique physical properties, nanobubbles exhibit distinct in vivo pharmacokinetics. We have shown that the first pass of the nanobubble bolus is usually accompanied by the appearance of a second bolus (wave) within a time range of about 15 minutes. Such phenomenon, to the best of our knowledge, has never been observed with conventional microbubbles and smaller molecular contrast agents used in MRI and CT. In a previous study, we showed the potential of this phenomenon in supporting cancer diagnosis. This study focuses on developing a new compartmental pharmacokinetic model that can be used to interpret the second-wave phenomenon. With this model, we can analyze more in-depth the roles of several physiological factors affecting the characteristics of the second-wave phenomenon.**

Index Terms—**Pharmacokinetic modeling, nanobubbles, contrast-enhanced ultrasound.**

I. INTRODUCTION

AS A WELL-ESTABLISHED imaging modality, contrast-enhanced ultrasound (CEUS) mostly utilizes stabilized microbubbles (MBs) as ultrasound contrast agents (UCA) to significantly increase vascular contrast [1]. Most types of MBs, whose diameter is 1–10 μm, are made of inert gas with low diffusivity encapsulated in a thin shell composed of biocompatible material, such as phospholipids or albumin [2].

The adoption of CEUS has enabled and facilitated a broad range of clinical applications, including cancer diagnosis [3], myocardial perfusion assessment [4], and drug delivery [5]. The utilization of MBs for cancer diagnosis is mostly based on the assessment of perfusion features of the abnormal microvasculature in the tumor as a result of angiogenesis [6]. After injecting MBs into the bloodstream, time-intensity curves (TIC) can be obtained by measuring the evolution of contrast enhancement as a function of time. Relevant hemodynamic parameters of clinical interests can be estimated from dedicated analysis of the measured TICs. However, the large diameter of MBs, which is comparable with the size of red blood cells, excludes the possibility of investigating the features in extravascular space. A reduction in MB diameter is expected to alter the intravascular nature of UCA and broaden the potential applications of CEUS. Nanobubbles (NBs), with a diameter of 100–500 nm, were recently developed as a new-generation UCA [7], [8]. Although being off resonance, several studies have demonstrated that NBs can produce adequate nonlinear contrast enhancement on clinical CEUS [9]. It was also shown that NBs can extravasate from the vasculature and enter the extravascular space during their relatively long-life span through the blood circulation [10], [11]. In the past decade, the reliability and potential applications of NB-based CEUS imaging (NB-CEUS) were increasingly recognized and utilized, especially for assessing vessel permeability and realizing molecular functional imaging [12], [13].

Given the 100–500 nm diameter of NBs, it is reasonable to expect that their in-vivo pharmacokinetics (PK) is distinct from those of conventional MBs and small molecular CA for MRI and CT. In comparison with the typical MB half-life of few minutes, the half-life of the latest NBs can exceed 1 hour [9]. In previous studies, researchers have investigated the prolonged retention effect caused by extravasation [13]. From a more general perspective, NBs can be regarded within the category of nanoparticles (NPs) [14]. In the last decade, a large number of studies were dedicated to the development of novel NPs and their applications in the fields of cancer localization and drug delivery [15], [16]. Advances in these fields impose increasing demands for comprehending and modeling the PK of these nanoscale particles. After intravenous administration, a NP usually experiences a meandering journey through the blood circulatory system and is exposed to several potential mechanisms of entanglement or clearance [17]. In

addition to NP diameter, the material, shape, surface charge, shell stiffness, and compressibility of the NP all play a role in altering the NP PK [18]. In this sense, the low density and high compressibility of NBs endue them unique PK in comparison with the typical NPs. In previous studies, one major focus was placed upon the transport of NBs in the tumor, in which microvasculature is characterized by an abnormal structure and higher permeability, as a result of angiogenesis [19]. Quantitative PK modeling of the NB distribution represents a powerful tool to investigate these complex mechanisms associated with angiogenesis.

The routine approach for PK modeling of NPs is by multicompartment modeling at the organ scale. For instance, it is common to represent each organ as an individual compartment when regarding the distribution of NPs over the whole body [20], [21]. In a specific organ, it is common to regard different anatomical structures or physiological functions as few separated compartments [22], [23]. Apart from these macroscale approaches, PK modeling of NBs can be also probed at the local scale, for instance, at the pixel level (the pixel size is usually few times smaller than the typical 100–500 μm spatial resolution in CEUS). With the local-scale PK modeling, one can obtain extensive information about the NB distribution and mobility [24]. This spatiotemporal information can facilitate the analysis of anatomical structures and the underlying physiological functions. However, to the best of our knowledge, there is by far no development of local-scale PK modeling of NBs or NPs.

Due to the fine spatial resolution ($\sim$100 μm) and high framerate ($\sim$100 fps), NB-CEUS can serve as an effective imaging modality to quantitatively assess the NB PK at the local scale. While investigating the NB PK by CEUS, we observed the occurrence of a second-wave phenomenon that is unique to NBs [25]. The first pass of the NB bolus is accompanied by the appearance of a second wave within 15 min after the first pass. This phenomenon has never been observed with conventional MBs. This so-called second-wave phenomenon, to our best knowledge, has not been described in the literature. In a previous article, we briefly described this second-wave phenomenon and suggested its potential clinical applications [25]. We hypothesized that this second-wave phenomenon is an inherent mechanism of NB PK within the tissue. In this paper, we propose a new PK model that can be used to interpret the second-wave phenomenon observed in NB-CEUS. Although this new PK model is difficult to be directly validated in experiments, it provides us with unique insights into the possible mechanisms of the second-wave phenomenon. To facilitate the quantification and visualization of the second-wave phenomenon, we also present a more empirical model that can be used to fit the NB-CEUS dataset at the pixel level.

II. Pharmacokinetic Modelling

A. The Journey of NBs

Once in the bloodstream, NBs begin a journey through several stages, including flow in the circulatory system, extravasation from the leaky vessels, accumulation in the extravascular space,
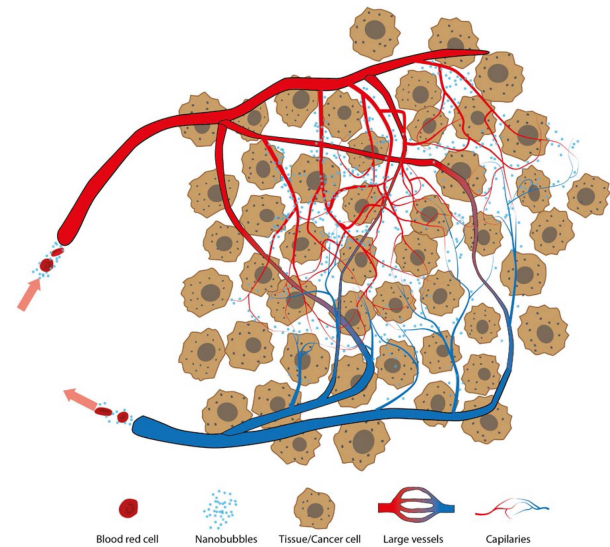

Fig. 1. Schematic illustration of important components in NBs intravascular transport and extravasation in the tumor microenvironment. The microvascular network of the tumor featured with tortuous morphology, excessive branching, abnormal shunts. After flowing into the vascular network from arteries (red vessels), the majority of NBs perfuse across the capillary bed, while some can directly travel through the vessel shunt reach veins directly (blue vessels). In this process, a portion of NBs extravasate from the leaky microvasculature and accumulate in the interstitial space. (Note: the relative size of presented objects does not indicate their real scales.).

entanglement with specific cells, and destruction due to either ultrasound exposure or natural dissolution or clearance. In the blood circulatory stage, NBs travel through different paths of the circulatory tree and reach a detection site at various times. The characteristics of NB perfusion in the circulatory tree differ between normal and cancerous microvasculature. In vessels with high permeability, NBs may cross the vessel wall and accumulate in the extravascular space. The efficiency of the so-called extravasation process is affected by multiple factors, including the vascular permeability and the local NB concentration in plasma. For solid tumors, because of the chaotic development of abnormal vasculature driven by angiogenesis, vascular permeability and density are highly heterogeneous [26]. For instance, vascular density in the periphery is usually higher than that in the tumor core [27].

Therefore, for PK modeling of NBs in the tumor, several factors, such as vascular structure, vascular permeability, and the extravascular environment, should be considered. Fig. 1 presents a schematic illustration of NB intravascular transport and extravasation in tumor microenvironment [17]. After flowing into the artery, the majority of NBs perfuse within the capillary bed. However, in the presence of blood shunts, which are a feature of cancer angiogenic vasculature [28], a portion of NBs can directly flow from large arteries to veins. In general, the transport of NBs in large vessels is faster, while the perfusion of NBs in the capillary bed is slower. Although there is a natural trend for NBs to further redistribute in the extravascular space, such diffusion process is opposed by a series of biological barriers and physiological conditions, e.g., high interstitial pressure, extracellular matrix, and the high cellular density (limited space
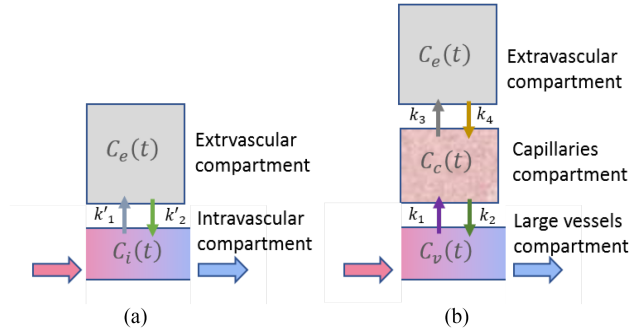
Fig. 2. Schematic diagram of ROI-based compartmental models. (a) is referred to as the two-compartment model, (b) is referred to as the three-compartment model.

between cancer cells) [17]. Previous studies have suggested that NP migration across the distance between two adjacent capillaries in the extravascular space, within a period of e.g., 1 h is extremely low [24].

B. Three-Layers Compartmental Model

The aforementioned description of NP transport establishes the basis for our NB PK modeling in an organ structure. In a conventional compartmental model representing the CA concentration, each compartment is defined as a well-mixed space in which the NBs have a uniform concentration $C(t)$. The most common model adopts two well-mixed compartments, i.e., intravascular and extravascular-extracellular compartments. This model is widely applied for PK modeling of small-molecular (typically < 20 nm) drugs a nd CAs. In this model, CA arrival at a certain site is assumed to be mainly driven by the arterial blood supply, while the perfusion across the microvasculature is not considered. As shown in Fig. 2(a), this so-called two-compartment model allows the exchange of NBs between the intravascular and extravascular spaces.

In comparison with the conventional small-molecule CAs, the flow of NBs in the capillary bed becomes less efficient and more complex due to their relatively larger diameter. It is thus reasonable to model differently the NB PK in the fast blood flow of large vessels and the relatively slower perfusion of smaller capillaries. Therefore, we divide the intravascular compartment into two separate compartments representing large-vessels and capillaries, respectively, as shown in Fig. 2(b). This model is thus referred to as three-compartment model. For the two-compartment and three-compartment models, NB concentrations in the intravascular compartment $C_i(t)$ and large-vessel compartment $C_v(t)$ are regarded as the input function, respectively. By solving the differential equation via Laplace transform, the two-compartment model describes $C_e(t)$ as a function of $C_i(t)$ by a convolution operator as

$$C_e(t) = k'_1 C_i(t) * e^{-k'_2 t}. \qquad (1)$$

In practice, because the actual intravascular and large-vessel volumes are difficult to be determined in a certain region of interest (ROI), it is common to introduce effective fractional volumes

as variables to reflect their weights on the total concentration as

$$C_t(t) = V_i C_i(t) + (1 - V_i) C_e(t)$$
$$= V_i C_i(t) + (1 - V_i) k'_1 C_i(t) * e^{-k'_2 t} \qquad (2)$$

for the two-compartment model.

Likewise, the total concentration for the three-compartments model is

$$C_t(t) = V_v C_v(t) + (1 - V_v)(C_c(t) + C_e(t))$$
$$= V_v C_v(t) + (1 - V_v)(a_{t1} C_v(t) * e^{-\lambda_1 t}$$
$$- a_{t2} C_v(t) * e^{-\lambda_2 t}). \qquad (3)$$

Here, V_i and V_v represent the effective fractions of intravascular volume and large-vessel volume in the investigated ROI or pixel/voxel, respectively. The detailed derivations of (1)–(3) and expressions of k_1, k_2, k'_1, k'_2, a_{c1}, a_{c2}, a_{t1}, a_{t2}, a_e, λ_1, and λ_2 are presented in Appendix A of the supplementary materials.

In these two models, there is one major underlying hypothesis: the mixture of NBs in each compartment is fast enough such that the time needed for distributing the NBs within each compartment space can be neglected. This hypothesis may be valid when considering the PK of small molecules. However, when we assess the NB PK, this assumption may no longer hold because of their larger size, leading to more prominent interaction with the capillary and extravascular structures that influences NB transport and diffusion, essentially slowing down NB migration. In the capillary bed, NB transport is affected by multiple factors, including the geometry, inner diameter, and density of the capillaries. In the extravascular space, we hypothesize that the NB diffusion is too low to assume instantaneous, perfect mixing across the extravascular space, especially for the higher cellular densities in malignant tissue.

Based on the above considerations, we hereby propose a new compartmental model by expanding both capillaries and extravascular compartments into several spatially-distributed compartments. Moreover, the large vessels can conceptually be classified as arteries, veins, and blood shunts to reflect their different roles in affecting the NB PK. As shown in Fig. 3, the three compartments illustrated in Fig. 2(b) are expanded along the horizontal dimension to N spatially-distributed compartments at the capillary and extravascular layers, respectively. For each compartment in the capillary layer, there is one corresponding compartment constructed in the extravascular space to represent the local NB exchange between capillary and extravascular spaces. Since the compartments are arranged in three layered cascades, this model is referred to as the three-layer model. The nth compartment at a certain layer is notated as n-<layer name> compartment, e.g., n-capillary represents the n th compartment within the capillary layer. At the bottom large-vessel layer, the NB concentrations in arteries and veins are separately regarded as two compartments. In the presence of arteriovenous shunts, which is an important biomarker of tumor angiogenesis, there is a direct connection between arteries and veins (see Fig. 1). This is taken into account by allowing for transport from the arterial to the venous compartments at a rate given by k_0 (see Fig. 3).
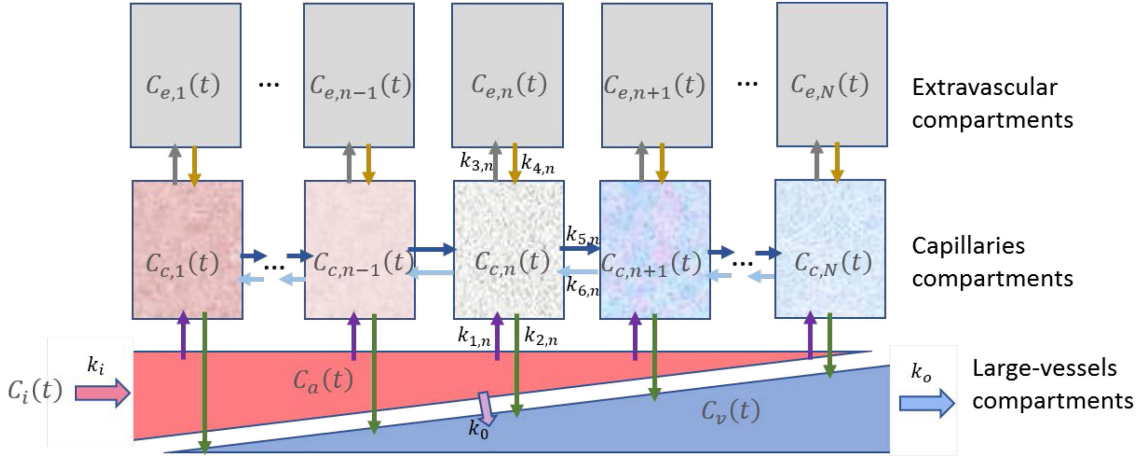
Fig. 3. Schematic diagram of the three-layer model. The bottom layer contains two compartments to represent the separate NB concentration in arteries (red) and veins (blue). The middle layer consists of N compartments arranged in a cascade to represent the spatially-distributed capillaries. The top layer consists of N compartments in a cascade to represent the extravascular space.

Since the three-layer model is made of multiple components with several parameters involved, the theoretical solution of this model is more complex than that of the aforementioned models with few compartments. We hereby introduce the state-space representation to facilitate the theoretical derivation and numerical computation. With the aid of matrix notation, we can present the analytical expression of the NB concentrations in each compartment. The details of this state-space representation are reported in Appendix B of the supplementary materials. Briefly, the essential step is to compile a sequence of concentrations $C_a(t), C_v(t), C_{c,n}(t), C_{e,n}(t)$ as a state vector $\boldsymbol{X}(t)$ containing $2N + 2$ elements:

$$
\begin{aligned}
\boldsymbol{X}(t) = [&C_a(t),\ C_v(t), \\
&C_{c,1}(t), \ldots, C_{c,n}(t), \ldots, C_{c,N}(t), \\
&C_{e,1}(t), \ldots, C_{e,n}(t), \ldots, C_{e,N}(t)]^T,
\end{aligned}
\tag{4}
$$

where N represents the number of compartments in the capillary and extravascular layers.

In the state-space representation, the derivative of $\boldsymbol{X}(t)$ is related to the linear combination of $\boldsymbol{X}(t)$ and the input $C_i(t)$:

$$
\dot{\boldsymbol{X}}(t) = \boldsymbol{A}\boldsymbol{X}(t) + \boldsymbol{B}C_i(t).
\tag{5}
$$

Here, $\boldsymbol{A}$ is a $(2N+2) \times (2N+2)$ matrix whose content is explicitly described in Appendix B (B8–B10) of the supplementary materials. To account for NB dissolution, we additionally introduce the parameter k_d (rate of NB dissolution); NB dissolution is mainly caused by NB interactions with the US waves and blood stream. By converting (5) into the Laplace domain, we obtain the transfer function in a matrix form as

$$
\begin{aligned}
\boldsymbol{X}(s)s &= \boldsymbol{A}\boldsymbol{X}(s) + \boldsymbol{B}C_i(s) \Rightarrow \boldsymbol{X}(s) \\
&= (s\boldsymbol{I} - \boldsymbol{A})^{-1}\boldsymbol{B}C_i(s).
\end{aligned}
\tag{6}
$$

In principle, by inverse transformation of the transfer function $\boldsymbol{X}(s)$ back into the time domain, we can obtain the analytical expression of the NB concentration over time in each compartment. However, as determining the analytical form of the matrix inverse $(s\boldsymbol{I} - \boldsymbol{A})^{-1}$ is complex, we derive its numerical approximation by propagating the discrete-time state-space equations by dedicated software implementation (MATLAB 2020a, MathWorks, Natick, MA) [29].

Similar to (2) and (3), the NB can be considered to be found in large vessels, capillaries, and extravascular space. Because the local distribution of arteries and veins differs over space, the effective fractional volumes of the arteries $V_{a,n}$ and veins $V_{v,n}$ are introduced to represent their relative contribution within a certain pixel/voxel space, respectively [23]. If we measure the local total NB concentration $C_t(t)$, including all the three layers and the spatially-distributed compartments, the measured concentration can be expressed as

$$
\begin{aligned}
C_t(t) = {}& V_a C_a(t) + V_v C_v(t) \\
&+ \sum_{n=1}^{N} [V_{c,n} C_{c,n}(t) + V_{e,n} C_{e,n}(t)].
\end{aligned}
\tag{7}
$$

In this way, we can construct an observation matrix $\boldsymbol{C}$ of size $1 \times (2N+2)$ with elements

$$
\begin{aligned}
\boldsymbol{C} = {}& [V_{a,n}, V_{v,n}, V_{c,1}, \ldots, V_{c,n}, \ldots, V_{c,N}, \\
& V_{e,1}, \ldots, V_{e,n}, \ldots, V_{e,N}].
\end{aligned}
\tag{8}
$$

Then, $C_t(t)$ can be calculated by

$$
C_t(t) = \mathcal{L}^{-1}\left\{ \boldsymbol{C}(s\boldsymbol{I} - \boldsymbol{A})^{-1}\boldsymbol{B}C_i(s) \right\},
\tag{9}
$$

where $\mathcal{L}^{-1}$ represents the Laplace inverse transform.

With this three-layer model, one can efficiently simulate the variation of NB concentration over space and different locations. By setting specific parameters, the effects of several factors, including intravascular transport, extravasation, blood shunts, and dissolution, can be analyzed and quantified. By properly matching the anatomy of an organ structure to the design of this three-layer model, one can better interpret the in-vivo PK of NBs, and possibly recognize biomarkers that can be used for diagnosis.

C. Empirical Model For Fitting Experimental Data

Although the above three-layer model provides a straightforward approach for interpreting the NB PK by simulating the evolution of the NB concentration over time, it faces challenges when being applied for fitting experimental NB-CEUS datasets. The primary challenge is the issue of overfitting: a large number of parameters ($6N$ transfer rates, i.e., k_i, $k_{2,n}$, k_i), the arbitrary input function $C_i(t)$, and unknown fractional volumes (which add $2N$ parameters) lead to too many degrees of freedom. In this sense, the utility of the proposed three-layer model for fitting the experimental data, e.g., pixel-based NB-CEUS data, is limited.

To overcome this limitation, we developed an empirical model that incorporates a fewer number of parameters while building on the same principles as the proposed three-layer model. It can be regarded as a simplification of the three-layer model, providing a relatively concise analytical expression that can be directly applied for fitting the in-vivo NB-CEUS data and estimating relevant practical parameters of pathophysiological relevance, such as the intensity and time of the second wave.

Without loss of generality, let us consider a simple one-dimensional scenario that only regards NB transport in the capillary layer as through an infinite tube [30]. The cascade of capillary compartments could be viewed as adjacent tube segments of length Δx [31]. If the transfer rates are the same for all the compartments, namely $k_{5,n} = k_5$, $k_{6,n} = k_6$, the differential equation for the n-capillary compartment can be simplified as

$$\frac{dC_n(t)}{dt} = k_5 C_{c,n-1}(t) + k_6 C_{c,n+1}(t) - (k_5 + k_6) C_{c,n}(t).$$
(10)

Introducing the local concentration $C(n\Delta x, t)$, with n indicating the compartment number and Δx the spatial extension of the compartment simplified in one dimension, (10) can be approximated as

$$\frac{dC(n\Delta x, t)}{dt} = (k_6 - k_5)\left[C((n+1)\Delta x, t) - C(n\Delta x, t)\right]$$
$$- k_5\left[C(n\Delta x, t) - C((n-1)\Delta x, t)\right.$$
$$\left. - C((n+1)\Delta x, t) + C(n\Delta x, t)\right].$$
(11)

If the length of each compartment is further reduced to the limit, we can obtain a continuous differential equation. By setting Δx to an infinitely small step dx and notating $x = ndx$, (11) becomes

$$\frac{dC(x,t)}{dt} = k_5\left[\frac{\partial C(x + dx/2, t)}{\partial x}dx - \frac{\partial C(x - dx/2, t)}{\partial x}dx\right]$$
$$+ (k_6 - k_5)\left[\frac{\partial C(x + dx/2, t)}{\partial x}dx\right].$$
(12)

Here, if we let

$$k_5 dx^2 = D,$$
$$(k_5 - k_6)dx = v,$$
(13)

and approximate

$$\frac{\partial C(x + dx/2, t)}{\partial x} - \frac{\partial C(x - dx/2, t)}{\partial x} = \frac{\partial}{\partial x}\left(\frac{\partial C(x,t)}{\partial x}\right)dx,$$
(14)

a concise equation can be derived:

$$\frac{\partial C(x,t)}{\partial t} = \frac{\partial}{\partial x}\left(D\frac{\partial C(x,t)}{\partial x}\right) - v\frac{\partial C(x,t)}{\partial x}.$$
(15)

This equation is known as the general convection-diffusion relation to model the mono-dimensional transport of NBs in a single vessel [30]. Here, $C(x,t)$ is the NB concentration at position x and time t, D represents the NB diffusion coefficient, and v represents the convection velocity that drifts the NBs along with the flux. This derivation suggests that the diffusion coefficient D is theoretically related to the transfer rate k_5, and the convection velocity v is proportional to the difference of the transfer rates $k_5 - k_6$. Notice that both D and v can be assumed to be locally constant and moved out of the derivative.

In the original definition, diffusion refers to the particle transport due to Brownian motion, which is mainly driven by heat and concentration gradients. In a microvascular network, the concept of diffusion can be extended to describe the dispersion of NBs across multipath trajectories in the microvasculature, also referred to as apparent diffusion [32]. One solution of (12) is the local density random walk (LDRW) model [33], which can be interpreted by a "random walk" of the NBs along the single vessel. By adopting specific boundaries conditions, the modified LDRW model (mLDRW) was further proposed to provide a local interpretation of the concentration variation at the detection site [3]:

$$C_{mLDRW}(t; t_0, \kappa, \mu) = AUC\sqrt{\frac{\kappa}{2\pi(t - t_0)}}e^{-\frac{\kappa(t - t_0 - \mu)^2}{2(t - t_0)}}.$$
(16)

Here μ represents the mean transit time, t_0 is the theoretical injection time, AUC denotes the area under the curve, and κ represents the local dispersion-related parameter given by $\kappa = v^2/D$, with v being the NB intravascular velocity and D the NB intravascular dispersion. In our application, the mLDRW model can be used not only to depict the NB flow in the capillary layer, but also to model the variation of NB concentration in the large vessels.

Regarding the NB concentration observed at one voxel, which may contain both large vessels and capillaries, the overall variation can be mainly ascribed to the NBs PK at two layers: the fast transport of NBs in the large vessels, and the slow perfusion in the capillary bed. In the case of high vessel permeability, a portion of NBs can extravasate from the capillaries. Similar to the derivations in (A4) and (A9) in the supplementary materials, the overall NB concentration should be calculated as the summation of four contributions: 1. concentration in capillaries, 2. concentration in large vessels, 3. the retention function of capillary concentration, 4. the retention function of large-vessel concentration.

We propose to analytically express the total NB concentration as the superimposition of two types of waves. The first wave corresponds to the fast transport in large vessels, and the second

wave represents the perfusion in the capillary bed. Specifically, each wave is modeled as the combination of the mLDRW and retention functions, represented by the convolution of the mLDRW function with an exponentially decaying function. The analytical expression of the resulting model, referred to as double-mLDRW model, is given as

$$
\begin{aligned}
C\left(t\right) = \alpha_1 & \left[C_{mLDRW}\left(t; t_0, \kappa_1, \mu_1\right)\right. \\
& \left. + \beta_1 C_{mLDRW}\left(t; t_0, \kappa_1, \mu_1\right) * e^{-\lambda t}\right] \\
+ \alpha_2 & \left[C_{mLDRW}\left(t; t_0, \kappa_2, \mu_2\right)\right. \\
& \left. + \beta_2 C_{mLDRW}\left(t; t_0, \kappa_2, \mu_2\right) * e^{-\lambda t}\right]. \quad (17)
\end{aligned}
$$

Here, the function $C_{mLDRW}(t; t_0, \kappa, \mu)$ represents the mLDRW model that describes the intravascular transport process; κ_1 μ_1, α_1 and β_1 represent the dispersion-related parameter, mean transit time, and the intensity scaling ratio of the retention function for the first wave, respectively. Likewise, κ_2, μ_2, α_2 and β_2 represent the corresponding parameters for the second wave. λ represents the decaying rate of the retention function. For facilitating the evaluation, we denote the maximum values of the first wave and the second wave as

$$
m_1 = \max\left\{\alpha_1\left[\begin{array}{c} C_{mLDRW}\left(t; t_0, \kappa_1, \mu_1\right) \\ + \beta_1 C_{mLDRW}\left(t; t_0, \kappa_1, \mu_1\right) * e^{-\lambda t}\end{array}\right]\right\} \quad (18)
$$

and

$$
m_2 = \max\left\{\alpha_2\left[\begin{array}{c} C_{mLDRW}\left(t; t_0, \kappa_2, \mu_2\right) \\ + \beta_2 C_{mLDRW}\left(t; t_0, \kappa_2, \mu_2\right) * e^{-\lambda t}\end{array}\right]\right\}, \quad (19)
$$

respectively. In addition, the time to peak of the first wave and the second wave are denoted by τ_1 and τ_2, respectively. In the above expressions, one can notice that the two waves share the same theoretical injection time, t_0, and decaying rate, λ, to provide a more realistic representation of the underlying flow-retention process and for mitigating the risk of overfitting. From the physiological perspective, t_0 is expected to be theoretically the same for the two waves since t_0 mainly represents the theoretical time needed for the NB to cover the distance from the injection to the detection site; the decaying rate λ of the retention function is mainly determined by the vascular permeability, which is also expected to be the same for the two waves.

III. MATERIAL AND METHODS

The aforementioned two models need to be evaluated experimentally. The double-mLDRW model is mainly applied for fitting the experimental NB-CEUS data. Through the model fitting, several parameters can be estimated to quantify and visualize the characteristics of the second-wave phenomenon. The three-layer model is mainly used for investigating the underlying mechanisms leading to the second-wave phenomenon and reproducing TICs that are comparable to the measured ones. The roles of relevant factors can be better analyzed by simulating the model with different parameters settings. In the rest of this section, we firstly describe the simulation of the three-layer model for reproducing the second-wave phenomenon. We then introduce the adopted animal model and NB-CEUS

acquisition protocols for demonstrating the second-wave phenomenon. Lastly, double-mLDRW model fitting is applied to the measured pixel-based TICs.

A. Application of the Three-Layer Model

The three-layer model was evaluated by setting different parameters to simulate the NB concentration across compartments. To keep it concise, we examined the roles of specific factors via iterative controlled simulation experiments: with regards to a specific factor, relevant parameters were set to different values, while keeping the other parameters at the default values. Overall, we compared the simulation results for evaluating five factors: 1) number of subdividing compartments (N), 2) Extravasation ($k_{3,n}$, $k_{4,n}$), 3) dispersion in the capillary bed ($k_{5,n}$, $k_{6,n}$), 4) convection in the capillary bed ($k_{5,n} - k_{6,n}$), 5) blood shunt (k_0), 6) NB diffusion rate (k_d). For each factor, the corresponding model parameters were changed for iterative simulations. The numerical simulation was implemented in MATLAB 2020a [29]. The details of the simulation parameter settings and simulation results of NB diffusion rate are presented in Appendix C of the supplementary materials.

In the evaluation of each factor, three aspects of the simulation results were inspected by comparing the variation of NB concentration over time. The first aspect is the formation of the second wave, e.g., the migration of NB distribution across compartments at the capillary and extravascular layers. Specifically, a series of $C_{c,n}(t)$ and $C_{c,n}(t) + C_{e,n}(t)$ are presented to illustrate the profile and timing of the second wave. The second aspect is the total $C_t(t)$ that integrates the NB concentrations from all compartments (matrix elements in C are set to one). The last aspect is the output $C_v(t)$ of the model, i.e., the NB concentration in the venous compartment.

In addition, the effect of fractional volumes on the overall NB concentration was also studied by setting different fractional volumes in the simulation with default parameters of dividing ten compartments. Three aspects of the simulation results were inspected. The first aspect is the combination of NB concentration in the arterial compartment and different sections in the capillary and extravascular layers. Specifically, three representative NB concentrations, $C_{t,a,early}(t)$, $C_{t,a,medium}(t)$ and $C_{t,a,late}(t)$, were respectively calculated to represent the combination of $C_a(t)$ and a subgroup of $C_{c,n}(t)$ and $C_{e,n}(t)$ from the left, middle, and right sections of the capillary and extravascular layers. Likewise, for the second aspect, three representative NB concentrations, $C_{t,v,early}(t)$, $C_{t,v,medium}(t)$ and $C_{t,v,late}(t)$ were calculated to combine $C_v(t)$ and a subgroup of $C_{c,n}(t)$ and $C_{e,n}(t)$ from the left, middle, and right sections of the capillary and extravascular layers. The third aspect aims at inspecting the effect of fractional volume on

$$
C_{t,a,medium}\left(t\right) = V_a C_a\left(t\right) + \left(1 - V_a\right) \sum_{n=5}^{7} \times \left[C_{c,n}\left(t\right) + C_{e,n}\left(t\right)\right]. \quad (20)
$$

Specifically, we set V_a to 0.05, 0.2 and 0.4 in $C_{t,a,medium}$, which is notated as $C_{t,V_a=0.05}(t)$, $C_{t,V_a=0.20}(t)$, and

$C_{t,V_a=0.40}(t)$, respectively. The expressions of these combined concentrations and details of the simulation settings are described in Appendix C of the supplementary materials.

B. Animal Model and NB-CEUS Acquisition

For preparing NBs, we utilized a recently developed NB whose shell composition is engineered to be highly stable to manifest a prolonged half-life in CEUS imaging. Readers can refer to [8] for more information on the NB preparation. The diameter distribution and concentration of NBs were measured to be 284 ± 96 nm and $4.07 \times 10^{11} \pm 2.45 \times 10^{10}$ NBs per mL (mean value $\pm$ standard deviation), respectively. Regarding the in-vivo CEUS experiment, seven 4–6-weeks-old mice were employed, handled according to a protocol approved by the Institutional Animal Care and Use Committee (IACUC) at Case Western Reserve University, and in accordance with all applicable protocols and guidelines. For each mouse, a dual-tumor model was initiated by subcutaneously injecting 1×10^6 prostate cancer cells in 100 μL Matrigel into the two flanks. This dual-tumor animal model was used in our previous study to analyze the prolonged retention effect with prostate-specific membrane antigen (PSMA) targeted nanobubbles [34]. In this dual-tumor model, the right PC3pip tumor overexpresses PSMA while the left PC3flu tumor does not. Apart from the PSMA expression, we hypothesized no relevant difference in the vasculature and morphology between the two types of tumors. Since only untargeted nanobubbles are used in this study, we consider the PK in the two types of tumors to be equivalent and make no distinction between the two types of tumor ROIs. Mice were examined daily until the tumor diameter reached 8 to 10 mm. Before acquiring CEUS images, mice were anesthetized by inhalation of 3% isoflurane with 1 L/min oxygen.

For acquiring NB-CEUS, 200-μL NBs were administered over 30 seconds via the tail vein using a 26 G catheter. A PLT-1204BT probe (central frequency, 12 MHz; MI, 0.1; dynamic range, 65 dB; gain, 70 dB; imaging frame rate, 1fps for 5 min and then 0.2fps for the rest time) c onnected to a Toshiba ultrasound machine (AplioXG SSA-790A, Toshiba Medical Imaging Systems, now Canon) was fixed to visualize the variation of contrast enhancement in the anesthetized mice. CEUS acquisitions of mouse dual tumors were performed so as to image the left tumor and the right tumor ROI in the same field of view. The CEUS image has a pixel size of 112 μm. The spatial resolution was estimated to be about 250 μm $\times$ 150 μm (lateral $\times$ axial) by measuring the average intensity profiles of several imaging points. Due to storage limitations in the US machine, the first 5 min the CE US loops were recorded at 1 Hz, afterward, the sampling rate was switched to 0.2 Hz. After about 30 min, we employed high-intensity flashes to destroy the remaining NBs. The experimental setup of the CEUS acquisition is illustrated in Fig. 4. After acquiring the CEUS loops, the evolution of the dB-scaled contrast enhancement over time was recorded at each pixel to obtain pixel-based TICs. To improve the signal-to-noise ratio, these TICs were spatially filtered by convolving the CEUS images with a 2D Gaussian kernel (Full-Width-at-Half-Maximum, 300 μm). The spatially filtered dB-scaled TICs
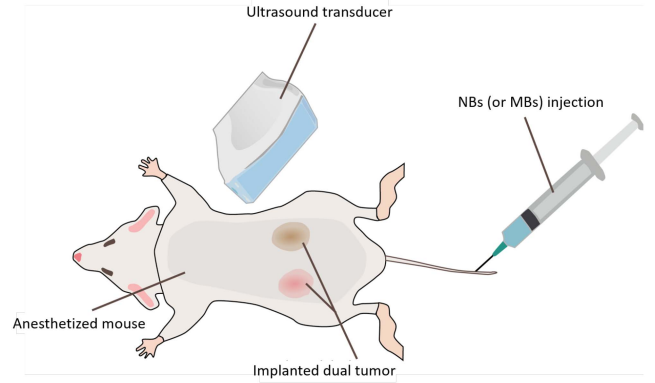

Fig. 4. Schematic illustration of the experimental setup. The male athymic nude mouse was anesthetized. A dual-tumor model was subcutaneously implanted in each limb. The ultrasound probe was fixated to keep two tumors in the same field of view. NB-CEUS loop was acquired by administering a 200-μL bolus NBs via the tail vein.

were then linearized into intensity-scaled TICs by reverting the dynamic-range compression in the CEUS setting [32]. An approximately linear relationship between the intensity and the local concentration of UCAs can be assumed [35]. These TICs were resampled at 1 Hz frequency and filtered by a low-pass filter with a passband 0.1 Hz frequency for further model fitting and analysis.

C. Application of the Double-mLDRW Model

Preprocessed pixel-based TICs were fitted by the double-mLDRW model. Model fitting was performed by a least-square fitting method using the trust-region reflective algorithm as implemented in the Python SciPy package [36]. For each parameter, the initial values, the upper bound, and lower bound were estimated based on the measured area under the curve (AUC), wash-out rate (WoR), time to peak (TTP), and peak enhancement (PE). Based on our observations, the range of μ_1 and μ_2 values were bounded between 1-2 min and 3–15 min, respectively. For t_0, an iterative search was implemented in a grid spanning from 45 s to 75 s in 1-s steps to search for the smallest squared error. Pixels with a maximum grey level lower than 3 were not included for the TIC fitting to guarantee sufficient signal-to-noise ratio. The goodness of the model fitting was quantified by the coefficient of determination R^2 as

$$R^2 = 1 - \frac{\| I_t(t) - I_e(t) \|}{\| I_e(t) - \overline{I_e} \|}. \tag{21}$$

Here, $I_e(t)$, $I_t(t)$, $\overline{I_e}$, and $\| \cdot \|$ represent the experimental TIC, the fitted TIC, the mean value of experimental TIC, and the Euclidean norm, respectively.

After fitting pixel-based TICs with the double-mLDRW model, parametric maps of τ_2, κ_2 λ, and $\log_{10}(m_2/m_1)$ were produced and visualized. τ_2 and κ_2 indicate the characteristics of the second wave in terms of time to peak and convective-dispersion PK. λ denotes the decaying rate which is supposed to be mainly affected by NB extravasation and microvasculature geometry. $\log_{10}(m_2/m_1)$ measures the peak intensity of the
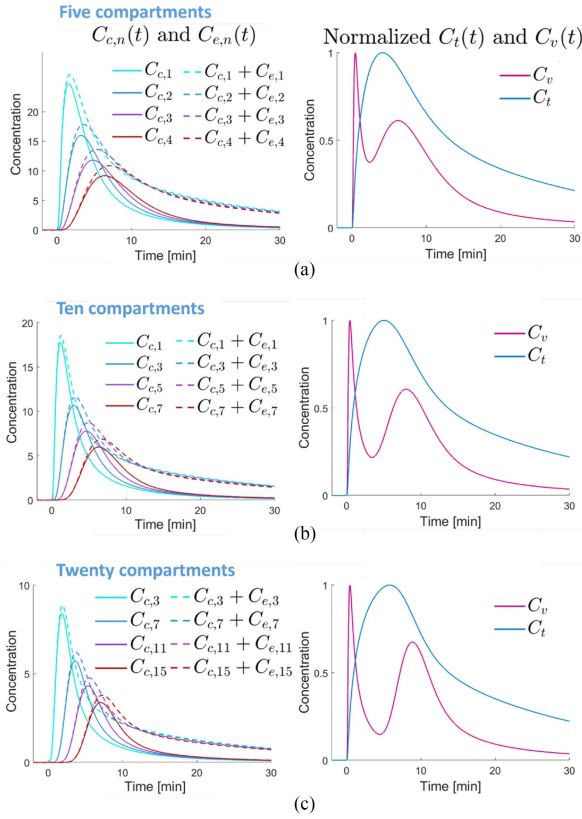
Fig. 5. Simulated results of NB concentration over time in case of five compartments (a, $N = 5$), ten compartments (b, default setting, $N = 10$), and twenty compartments (c, $N = 20$). In each case, the left subfigure presents the profiles of $C_{c,n}(t)$ and $C_{c,n}(t) + C_{e,n}(t)$ to indicate the movement and transform of the second wave; the right subfigure presents the profiles of $C_v(t)$ and $C_t(t)$.
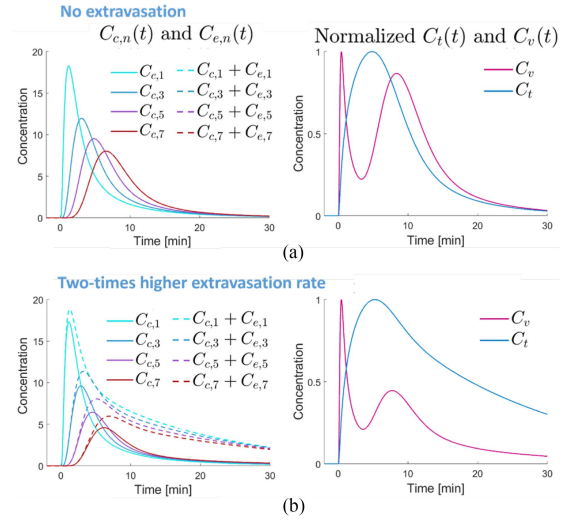

Fig. 6. Simulated results of NB concentration over time in the cases of no extravasation (a, $k_{3,n} = 0$, $k_{4,n} = 0$) and extravasation rate two times higher (b, $k_{3,n} = 2 \times 10^{-3}$, $k_{4,n} = 5 \times 10^{-4}$) than the default case in Fig. 5(b, $k_{3,n} = 1 \times 10^{-3}$, $k_{4,n} = 2.5 \times 10^{-4}$). In each case, the left subfigure presents the profiles of $C_{c,n}(t)$ and $C_{c,n}(t) + C_{e,n}(t)$ to indicate the movement and transform of second wave; the right subfigure presents the profiles of $C_v(t)$ and $C_t(t)$.
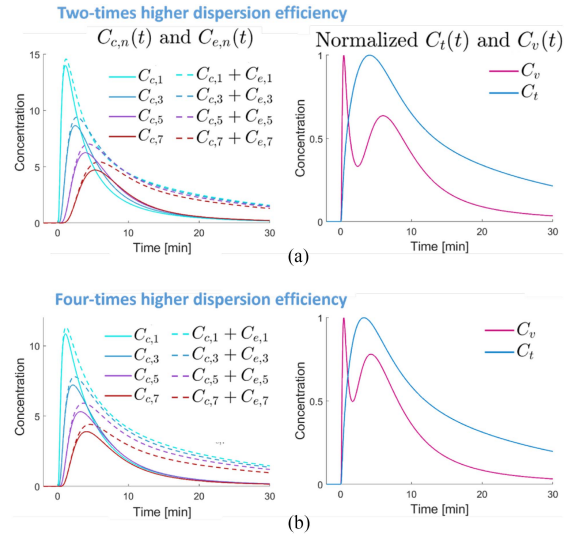

Fig. 7. Simulated results of NB concentration over time in the cases of dispersion efficiency two times (a, $k_{5,n} = 4 \times 10^{-2}$, $k_{6,n} = 2 \times 10^{-2}$) and four times (b, $k_{5,n} = 8 \times 10^{-2}$, $k_{6,n} = 6 \times 10^{-2}$) higher than default case in Fig. 5(b, $k_{5,n} = 2 \times 10^{-2}$, $k_{6,n} = 0$). In each case, the left subfigure presents the profiles of $C_{c,n}(t)$ and $C_{c,n}(t) + C_{e,n}(t)$ to indicate the movement and transform of second wave; the right subfigure presents the profiles of $C_v(t)$ and $C_t(t)$.

second wave relative to the first wave. We additionally regarded the Kolmogorov–Smirnov statistic (D) to measure the distance between the cumulative probabilities of the parameter distributions for malignant and benign tissue [37]. A parameter with D > 0.25 is regarded to be significantly different.

IV. RESULTS

A. Effects of Number of Compartments and Extravasation

In Fig. 5, the simulation results using a different number of cascaded compartments are presented. In comparison with the default setting, subdividing the ROI into ten compartments (Fig. 5(b)), simulating twenty compartments (c) presents similar profiles on almost all the simulated concentrations. Such similarity is relatively less when comparing the default setting and the case of five compartments (Fig. 5(a)). In the profile of $C_v(t)$, the valley between two waves becomes more prominent if there is a larger number of compartments.

Fig. 6 presents the simulation results of different extravasation rates. In comparison with the default setting (Fig. 5(b)), the case of no extravasation presents a relatively more intense second wave and faster decaying trend on the simulated concentration profiles. On the contrary, when the extravasation rate is twice

higher, a less intense second wave and slower decaying trend on the simulated profiles were observed.

B. Effects of Dispersion Efficiency, Convection Efficiency, and Blood Shunts

Fig. 7 presents the simulation results for different dispersion efficiencies. In comparison with the default setting (Fig. 5(b)), dispersion two times higher (Fig. 7(a)) produces a relatively
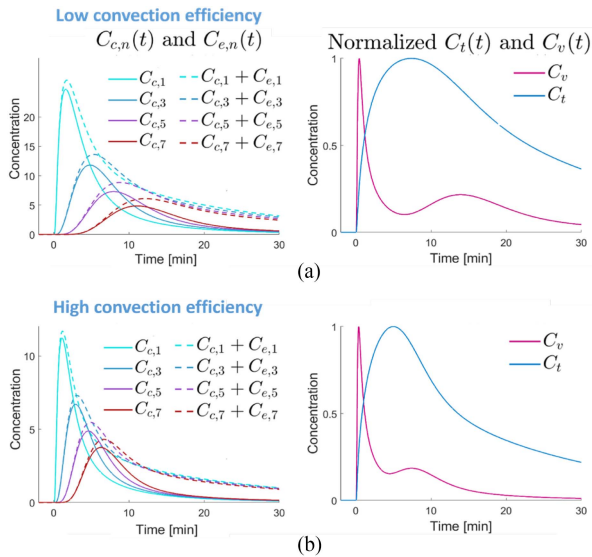
Fig. 8. Simulated results of NB concentration over time in the cases of low convection efficiency (a, $k_{5,n} = 1 \times 10^{-2}$, $k_{6,n} = 0$) and high convection efficiency (b, $k_{5,n} = 4 \times 10^{-2}$, $k_{6,n} = 0$) in comparison with the default case of moderate convection efficiency in Fig. 5(b, $k_{5,n} = 2 \times 10^{-2}$, $k_{6,n} = 0$). In each case, the left subfigure presents the profiles of $C_{c,n}(t)$ and $C_{c,n}(t) + C_{e,n}(t)$ to indicate the movement and transform of second wave; the right subfigure presents the profiles of $C_v(t)$ and $C_t(t)$.
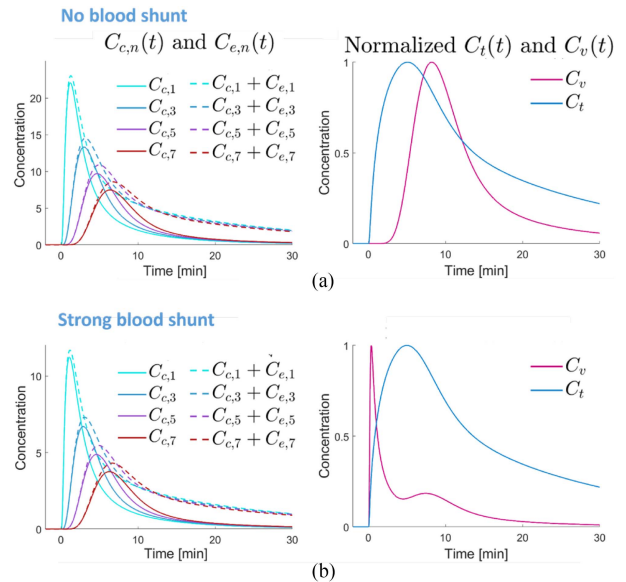

Fig. 9. Simulated results of NB concentration over time in the cases of no blood shunt (a, $k_0 = 0$) and strong blood shunt (b, $k_0 = 0.1$) in comparison with the default case of moderate blood shunt in Fig. 5(b, $k_0 = 2.5 \times 10^{-2}$). In each case, the left subfigure presents the profiles of $C_{c,n}(t)$ and $C_{c,n}(t) + C_{e,n}(t)$ to indicate the movement and transform of second wave; the right subfigure presents the profiles of $C_v(t)$ and $C_t(t)$.

earlier second wave on the simulated concentration profiles. Likewise, when the dispersion is four times higher (Fig. 7(b)), earlier second waves can be observed in the simulated profiles. With an earlier second wave, the separation of the first and second wave becomes less clear in the profile of $C_v(t)$. In Fig. 8, the simulation results for varying convection efficiencies are presented. In comparison with the default setting (Fig. 5(b)), lower convection produces a relatively less intense, broader, and more delayed second wave in the simulated concentration profiles. Fig. 9 presents the simulation results in the absence of blood shunt and with extensive blood shunts. In comparison with the default setting (Fig. 5(b)), in the absence of blood shunts (Fig. 9(a)), only the second wave is observed in the simulated profiles of $C_v(t)$. The simulation result in Fig. 9(b) shows that the second wave is relatively less intense in the profile of $C_v(t)$ if extensive blood shunts exist. Overall, the presence of blood shunts does not significantly affect the shape and transport of the second wave in the capillaries and extravascular layers.

C. Effects of Fractional Volume

Fig. 10 presents the simulation results by setting different fractional volumes when combining the NB concentrations from specific compartments. The profiles in Fig. 10(a), (b) show that the second wave appears at a gradually increasing time delay when combining the NB concentrations from the left, middle and right sections of the capillary and extravascular layers. The relative intensity of the second wave is higher in the combination with venous compartment. Using different fractional volumes, the profiles in Fig. 10(c) show that the relative intensity of the

second wave is highly dependent on the proportions of NB concentrations from various compartments.

D. Model Fitting of the Second-Wave Phenomenon

The model-fitting result of one mouse case is shown in Fig. 11(a)–(d). The second-wave phenomenon can be observed in the majority of pixel-based TICs from either malignant or benign tissues. The parametric maps of $\log_{10}(m_2/m_1)$ and λ both manifest differences between the tumor lesion and benign tissue outside the tumor. Fig. 11(e), (f) present the histograms of the parameter values over malignant and benign tissues from seven mice. Among the analyzed parameters, significantly higher λ values (D > 0.281) and significantly lower $\log_{10}(m_2/m_1)$ values (D > 0.254) were obtained in tumor ROIs compared to the surrounding ROIs of benign tissues. The corresponding statistic D values of τ_2 and κ_2 are 0.051 and 0.157, respectively. Regarding the goodness of model fitting, 86% of pixel-based TICs from seven mice were well fitted with the double-mLDRW model with $R^2 > 0.9$.

V. DISCUSSION

A. Second-Wave Phenomenon of NB PK

As an alternative modality to CT and MRI, CEUS is a competitive diagnostic tool for enhancing specific organ structures with several advantages, such as flexibility, cost-effectiveness, moderately high spatial resolution, and high temporal frame rate. The development of NBs as a new-generation UCA opens up a new avenue for CEUS by enabling the assessment of extravasation and the realization of ultrasound molecular imaging. NB is also
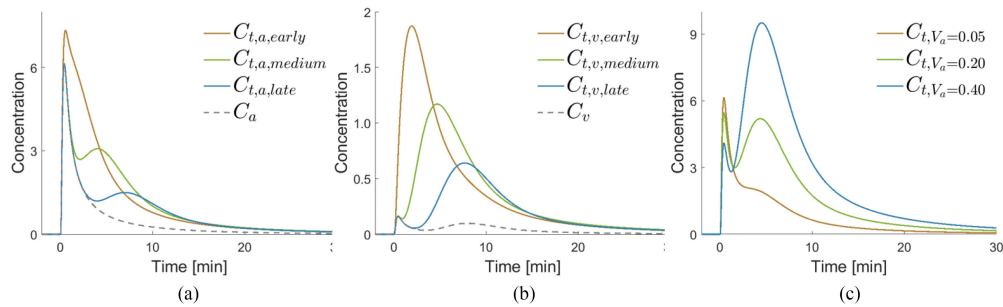
Fig. 10. Simulated results of the total NB concentration accounting for the contribution of different layers and compartments at varying volume fractions: a subgroup of $C_{c,n}(t) + C_{e,n}(t)$ combined with either $C_a(t)$ (a, c) or $C_v(t)$ (b). (a) presents the profiles of $C_a(t)$, $C_{t.a.early}(t)$, $C_{t.a.medium}(t)$, and $C_{t.a.late}(t)$ to indicate the different appearance of the second wave; (b) presents the profiles of $C_v(t)$, $C_{t.v.early}(t)$, $C_{t.v.medium}(t)$, and $C_{t.v.late}(t)$ to indicate the different appearance of the second wave; (c) presents the profiles of different $C_{t.a.medium}(t)$ with a specific volume fraction V_a to indicate the effect of different fractional volumes.
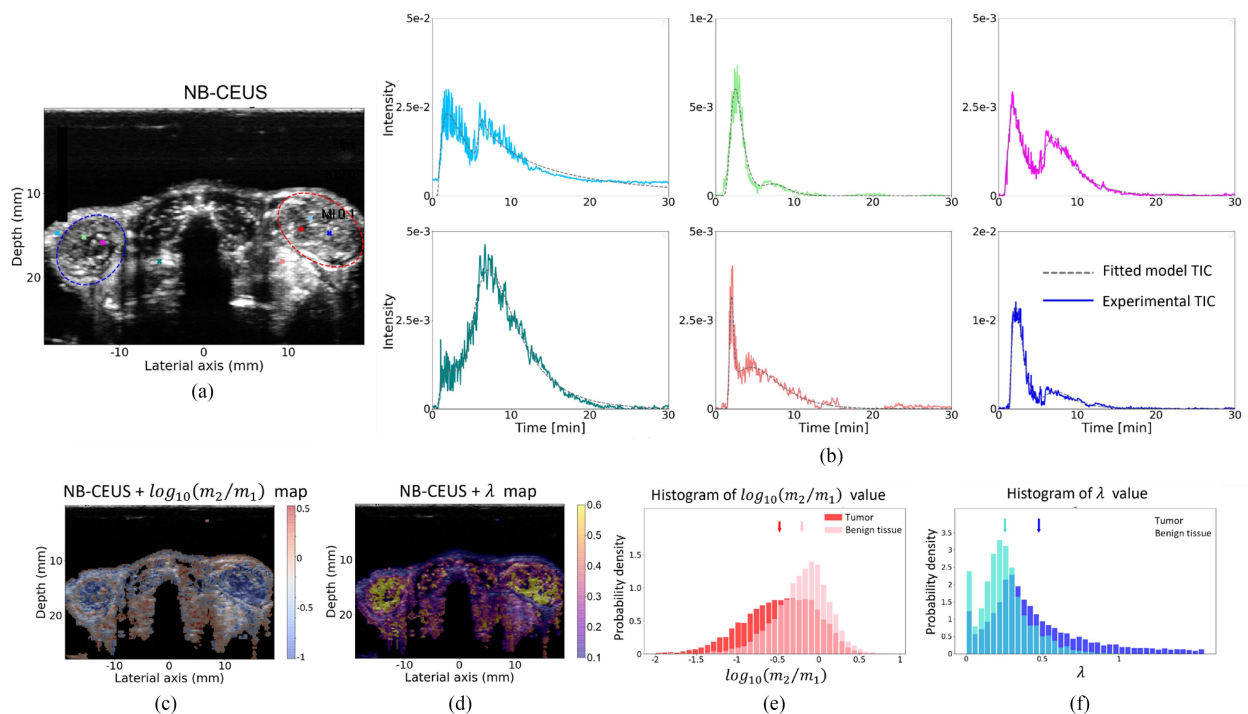

Fig. 11. An example of pixel-based TICs and parametric maps in a dual-tumor mouse model. (a) presents the maximum intensity projection of the NBs-CEUS loop, with the left and right tumor ROIs delineated in blue and red, respectively. In (b), a series of experimental pixel-based TICs (colored solid lines) and corresponding model fit (gray dashed lines) are extracted from different locations which are indicated by the corresponding colored dots in (a). The scales of the y-axis vary between subfigures in (b). (c) and (d) present the overlays of the parametric maps of $log_{10}(m_2/m_1)$ and λ upon the NB-CEUS projection image, respectively. (e) and (f) present the histograms of the estimated parameters $log_{10}(m_2/m_1)$ and λ between the tumor and benign tissue, with the mean values indicated by corresponding markers.

regarded as a special category of NP-based pharmaceuticals and CA. Previous analyses of the PK of NPs were mostly conducted at the organ level and long-time scale (across hours or days), without considering the local and short-term characteristics of the NP PK. Featured with fine spatial resolution and high frame rate, CEUS can serve as an effective imaging modality for assessing the PK of NBs.

In a previous work [25], we observed a unique second-wave phenomenon mainly occurring in the time range of 3 to 15 min after UCA injection. The peak intensity of the second wave can often exceed the peak intensity of the first wave. To the best of our knowledge, this second-wave phenomenon has not been

described in the literature about NPs and NBs. In conventional contrast-enhanced MRI and CT with small-molecular CA, the profile of pixel-based TICs is typically composed of a swift rising phase and a monotonous slowly-decaying or plateau phase. In MB-CEUS, a second rise of contrast due to blood recirculation mainly occurs within 1 min after the first pass. Typically, the intensity of this recirculation wave is 5-fold lower than the intensity of the first wave [38]. Therefore, we deduced this second wave is more likely to be due to the inherent in-vivo PK of the NBs within the organ structures, rather than blood recirculation through the full circulatory system. Our initial hypothesis is that the second wave mainly represents NB perfusion in the capillary

bed and the extravascular spaces, while the first wave is mainly due to NB transport in large vessels. Going beyond qualitative or semi-quantitative analysis, this work focuses on developing new PK models that can be used to interpret and quantify the second-wave phenomenon. With the proposed PK models, we can further support the hypothesis on interpreting the formation of the second-wave phenomenon, which has the potential to become an important biomarker for future clinical applications.

A three-layer model was developed by expanding the conventional multi-compartment model, in which each compartment represents the variation of NB concentration in a single organ structure, e.g., in a large vessel, capillaries, and extravascular spaces. In previous studies, few compartments were mostly employed to interpret the in-vivo PK of small-molecular particles (diameter < 20 nm). Their small diameter allows these particles to efficiently mix in both intravascular and extravascular spaces. In this sense, instantaneous homogenous mixing may be a valid assumption in each compartment. When utilizing 100–500 nm-diameter NBs, the efficiency of the intravascular transport and extravascular diffusion is reduced by enhanced interactions with the surrounding structures, especially in the capillary bed and the extravascular space. In order to account for slower capillary transport and extravascular diffusion, we propose to extend the capillary and the extravascular compartments by representing them as layers composed by a cascade of several compartments. This model design is in line with the hypothesis that the first wave and the second wave can be ascribed to the different NB PK in the large vessels and capillaries, respectively. If we observe the variation of NB concentration over time within a pixel, which can enclose arteries, capillaries, and veins, the occurrence of two waves can be explained by the superimposition of the first and second waves that respectively occur in arteries, veins, and capillaries. In the presence blood shunts, the NB concentration in the veins can also show two recognizable waves. It can also be noticed that the second-wave phenomenon is still prominent in the absence of extravasation. This suggests that the extravasation is not an essential factor in forming the second wave in NB-CEUS. Yet, this phenomenon has only been observed with NBs and not with MBs. With about ten-fold larger diameters than NBs, MBs are known not to extravasate. MBs are also expected to be less effective compared to NBs in the perfusion of the capillary bed, which can explain why a second wave cannot be observed. Moreover, because the typical life span of MBs is limited to 2 to 10 minutes in the blood circulation (which can be further reduced to < 1 minute when being exposed to acoustic waves) [38], [39], this relatively short period of contrast enhancement is not sufficient to observe a second-wave phenomenon for MBs.

B. The Simulation of Three-Layer Model

Using the three-layer cascade model and a state-space representation, we successfully reproduce the formation and time kinetics of the second wave via numerical simulation. By observing the movement and transformation of $C_{c,n}(t)$, we can confidently hypothesize that the second wave mainly represents the slow transport of NBs in the capillaries. The more empirical

double-mLDRW model, which was developed as a simplified version of the three-layer model, shows a good fitting with the experimental data (86% with $R^2 > 0.9$). This high fitting accuracy indirectly supports the validity of the three-layer model in revealing the mechanism of the second-wave phenomenon. Although there are a large number of parameters in the design of the three-layer model, the majority of the parameters were set to a fixed value (e.g., $k_{1,n} = 0$, $k_{2,n} = 0$, for $2 \leq n \leq N-1$; $k_{3,n} = k_{4,n}$, for all n) in the simulation to limit the degrees of freedom. Since most parameters have their specific physical meanings, the selection of parameter settings was primarily based on realistic considerations. For instance, the default dissolution rate $k_d = 5.56 \times 10^{-4}\ s^{-1}$ corresponds to the typical 21 minutes half-life of NBs; the default $k_{5,n}\ -\ -k_{6,n} = 0.02\ s^{-1}$ (for $1 \leq n \leq N-1$, $N = 10$) considers the average convection velocity of 0.1 mm/s to move through approximately 40 mm topological distance in the capillary bed. Nevertheless, the validity of these parameter settings needs to be further validated by experiments.

The simulation of different numbers of compartments shows that a default setting of simulating ten compartments does not produce significantly different results in comparison with twenty compartments, which is supposed to provide more accurate modeling of the NB transport in the capillaries. Reducing the number of compartments to five produces results that differ from those when using twenty compartments. For instance, the valley between two waves becomes less prominent in the TIC of veins. If the number of compartments is further reduced to two or one, the second-wave phenomenon is expected to vanish, as suggested in [23], [40]. This is because the slow NB perfusion in the capillary bed needs to be modeled by a large number of connected compartments, with each representing the relatively independent capillary section. The simulation of blood shunts suggests that a prominent second-wave phenomenon found in veins could be a direct indicator of existing blood shunts, which is an important biomarker for diagnosing tumors [41]. These results also suggest that the time delay and relative intensity of the second wave are highly dependent on the location of the ROI, as also confirmed by the TICs measured in vivo (Fig. 11). However, when considering the total NB concentration $C_t(t)$ from all compartments, the second-wave phenomenon tends to become less noticeable. This derives from the summation of several second waves with different delays and intensities. The absence of second-wave phenomenon is also observed in the total TIC of an entire tumor, liver, or kidney, as shown in our previous work [13]. The detailed analyses of the simulation results are presented in Appendix C of the supplementary materials. Overall, these simulation results and derivations, albeit not validated in experiments, provide a model for interpreting the formation and characteristics of the second-wave phenomenon.

C. Fitting the Second-Wave Phenomenon With Double-mLDRW Model

Although the three-layer model reproduces successfully the second-wave phenomenon, the large number of parameters in this complex model limits its application for fitting the

experimental data due to the large number of parameters and related risk of over-fitting. Instead, we derived the empirical double-mLDRW model with fewer parameters for fitting the in-vivo experimental data. The estimation of these parameters can provide us with relevant information and quantification about the second-wave phenomenon. Our results show that the estimated $\log_{10}(m_2/m_1)$ and λ values are significantly different between malignant and benign tissues. This suggests that a relatively weaker second-wave phenomenon and faster decaying rate of the NB concentration are prominent features of cancerous tissues in comparison with benign tissues. The relatively weaker second-wave phenomenon can probably be ascribed to the abnormal tumor vascular structures as a result of angiogenesis. Different from the normal vasculature that exhibits a regular branching structure, the tumor vasculature is usually featured with tortuous morphology, excessive branching, abnormal shunts, heterogeneous flow, and increased leakage to the extravascular space [41]. As suggested in the simulation of the three-layer model, the second wave is less intense for high extravasation and large blood shunts. This could probably explain the overall lower estimated $\log_{10}(m_2/m_1)$ values in the tumor, where leaky vessels and blood shunts are present. For the high λ values in the tumor, there are two possible explanations. The first possible mechanism for the relatively higher decaying rate of NB concentration is the higher ultrasound exposure of the NBs which have extravasated and been trapped in the interstitial space or in small capillaries. Secondly, the faster decaying rate can probably be also explained by the excessive branching structure of the tumor microvasculature, which facilitates a faster wash-out process, even though extravasation from leaky vessels can suppress the decaying trend. Overall, our preliminary results with the double-mLDRW model show promise for applying the second-wave phenomenon for clinical diagnostics. With about ten-fold smaller diameters than MBs, NBs can be used to assess vascular permeability and realize effective molecular imaging of biomarkers in the extravascular space [34]. The detailed analyses of vascular permeability, extravascular specific binding, NB perfusion, and their roles in the second-wave phenomenon can aid in the detection of tumors and diagnosis of different types of tumors.

D. Limitations and Outlooks

Although the proposed two models provide unique insights into the second-wave phenomenon, many aspects still require future investigation. Primarily, both the three-layer and double-mLDRW models can be further improved by incorporating more detailed biophysical information, e.g., the vascular network topology. The validity of the three-layer model and the underlying hypothesis needs to be thoroughly investigated by experiments. Secondly, the in-vivo results presented in this study are still preliminary and limited to non-orthotopic subcutaneous tumors in mice. It is of practical significance to examine the second-wave phenomenon presented in various structures, including different types of tumors, kidneys, liver, and spleen, and other (larger) animals. Thirdly, given the potential of utilizing targeted NBs in ultrasound molecular imaging, the effect of specific binding of targeted NBs in the extravascular space is worth being investigated by adapting the three-layer model to account for binding and by fitting the double-mLDRW model in in-vivo experiments with targeted NBs. Furthermore, the mechanism underlying the second-wave phenomenon needs to be further validated and investigated via experiments. Future studies should include the immunohistological analysis of ex-vivo tumor tissue to allow correlating the proposed PK parameters, obtained by in-vivo imaging, with the validated ex-vivo tumor biomarkers. Lastly, future works will investigate if the second-wave phenomenon observed in NB-CEUS also applies to the other types of NPs.

VI. Conclusion

In this study, we presented two novel models for interpreting the unique second-wave phenomenon observed in NB-CEUS. The complex three-layer model can be utilized to simulate the second-wave phenomenon and analyze the roles of relevant factors. The double-mLDRW model, although simpler and requiring stronger assumptions, allows for accurate fitting of the experimental data leading to the estimation of several parametric maps to quantify and visualize the in-vivo PK of NBs. Our result supports that the second-wave phenomenon is affected by a number of physiological factors, and is promising to be utilized in relevant clinical applications.

References

[1] P. Frinking et al., "Three decades of ultrasound contrast agents: A review of the past, present and future improvements," *Ultrasound Med. Biol.*, vol. 46, no. 4, pp. 892–908, 2020.

[2] D. Cosgrove, "Ultrasound contrast agents: An overview," *Eur. J. Radiol.*, vol. 60, no. 3, pp. 324–330, 2006.

[3] M. P. Kuenen, M. Mischi, and H. Wijkstra, "Contrast-ultrasound diffusion imaging for localization of prostate cancer," *IEEE Trans. Med. Imag.*, vol. 30, no. 8, pp. 1493–1502, Aug. 2011.

[4] K. Wei et al., "Quantification of myocardial blood flow with ultrasound-induced destruction of microbubbles administered as a constant venous infusion," *Circulation*, vol. 97, no. 5, pp. 473–483, 1998.

[5] K. Ferrara, R. Pollard, and M. Borden, "Ultrasound microbubble contrast agents: Fundamentals and application to gene and drug delivery," *Annu. Rev. Biomed. Eng.*, vol. 9, pp. 415–447, 2007.

[6] M. Kuenen et al., "Contrast-ultrasound dispersion imaging for prostate cancer localization by improved spatiotemporal similarity analysis," *Ultrasound Med. Biol.*, vol. 39, no. 9, pp. 1631–1641, 2013.

[7] R. H. Perera et al., "Ultrasound imaging beyond the vasculature with new generation contrast agents," *Wiley Interdiscipl. Rev.: Nanomedicine Nanobiotechnology*, vol. 7, no. 4, pp. 593–608, 2015.

[8] R. H. Perera et al., "Improving performance of nanoscale ultrasound contrast agents using N, N-diethylacrylamide stabilization," *Nanomedicine: Nanotechnology, Biol. Med.*, vol. 13, no. 1, pp. 59–67, 2017.

[9] H. Wu et al., "Acoustic characterization and pharmacokinetic analyses of new nanobubble ultrasound contrast agents," *Ultrasound Med. Biol.*, vol. 39, no. 11, pp. 2137–2146, 2013.

[10] C. Pellow et al., "Concurrent visual and acoustic tracking of passive and active delivery of nanobubbles to tumors," *Theranostics*, vol. 10, no. 25, 2020, Art. no. 11690.

[11] H. Wu et al., "Time-intensity-curve analysis and tumor extravasation of nanobubble ultrasound contrast agents," *Ultrasound Med. Biol.*, vol. 45, no. 9, pp. 2502–2514, 2019.

[12] H. Yang et al., "Nanobubble–Affibody: Novel ultrasound contrast agents for targeted molecular ultrasound imaging of tumor," *Biomaterials*, vol. 37, pp. 279–288, 2015.

[13] R. Perera et al., "Contrast enhanced ultrasound imaging by nature-inspired ultrastable echogenic nanobubbles," *Nanoscale*, vol. 11, no. 33, pp. 15647–15658, 2019.

[14] M. De, P. S. Ghosh, and V. M. Rotello, "Applications of nanoparticles in biology," *Adv. Mater.*, vol. 20, no. 22, pp. 4225–4241, 2008.

[15] E. Blanco, H. Shen, and M. Ferrari, "Principles of nanoparticle design for overcoming biological barriers to drug delivery," *Nature Biotechnol.*, vol. 33, no. 9, pp. 941–951, 2015.

[16] D. P. Cormode, P. C. Naha, and Z. A. Fayad, "Nanoparticle contrast agents for computed tomography: A focus on micelles," *Contrast Media Mol. Imag.*, vol. 9, no. 1, pp. 37–52, 2014.

[17] J. W. Nichols and Y. H. Bae, "Odyssey of a cancer nanoparticle: From injection site to site of action," *Nano today*, vol. 7, no. 6, pp. 606–618, 2012.

[18] R. Toy et al., "The effects of particle size, density and shape on margination of nanoparticles in microcirculation," *Nanotechnology*, vol. 22, no. 11, 2011, Art. no. 115101, doi: 10.1088/0957-4484/22/11/115101.

[19] V. Torchilin, "Tumor delivery of macromolecular drugs based on the EPR effect," *Adv. Drug Del. Rev.*, vol. 63, no. 3, pp. 131–135, 2011.

[20] P. Dogra et al., "Mathematical modeling in cancer nanomedicine: A review," *Biomed. Microdevices*, vol. 21, no. 2, pp. 1–23, 2019.

[21] H. Jones and K. Rowland-Yeo, "Basic concepts in physiologically based pharmacokinetic modeling in drug discovery and development," *CPT: Pharmacometrics Syst. Pharmacol.*, vol. 2, no. 8, pp. 1–12, 2013.

[22] S. Sourbron, "A tracer-kinetic field theory for medical imaging," *IEEE Trans. Med. Imag.*, vol. 33, no. 4, pp. 935–946, Apr. 2014.

[23] S. Turco, H. Wijkstra, and M. Mischi, "Mathematical models of contrast transport kinetics for cancer diagnostic imaging: A review," *IEEE Rev. Biomed. Eng.*, vol. 9, pp. 121–147, 2016.

[24] A. d'Esposito et al., "Computational fluid dynamics with imaging of cleared tissue and of in vivo perfusion predicts drug uptake and treatment responses in tumours," *Nature Biomed. Eng.*, vol. 2, no. 10, pp. 773–787, 2018.

[25] C. Chen et al., "The unique second wave phenomenon in contrast enhanced ultrasound imaging with nanobubbles," *Scientific Rep.*, vol. 12, no. 1, pp. 1–12, 2022. [Online]. Available: https://assets.researchsquare.com/files/rs-1247285/v1_covered.pdf?c=1642457682%20

[26] N. Charnley, S. Donaldson, and P. Price, *Imaging Angiogenesis*, vol. 467, 2nd ed. New York, NY, USA: Humana Press, 2009.

[27] D. A. I. Fukumura et al., "Tumor microvasculature and microenvironment: Novel insights through intravital imaging in pre-clinical models," *Micro-circulation*, vol. 17, no. 3, pp. 206–225, 2010.

[28] R. K. Jain, "Determinants of tumor blood flow: A review," *Cancer Res.*, vol. 48, pp. 2641–2658, 1988.

[29] The Math Works, Inc. MATLAB. Version 2020a, The Math Works, Inc., Computer Software, 2020. [Online]. Available: www.mathworks.com/

[30] G. Taylor, "Dispersion of soluble matter in solvent flowing slowly through a tube," *Proc. Roy. Soc. London A*, vol. 219, no. 1137, pp. 186–203, 1953.

[31] M. Mischi, J. A. Den Boer, and H. H. M. Korsten, "On the physical and stochastic representation of an indicator dilution curve as a gamma variate," *Physiol. Meas.*, vol. 29, no. 3, 2008, Art. no. 281.

[32] M. Arditi et al., "A new formalism for the quantification of tissue per-fusion by the destruction-replenishment method in contrast ultrasound imaging," *IEEE Trans. Ultrasonics, Ferroelect., Freq. Control*, vol. 53, no. 6, pp. 1118–1129, Jun. 2006.

[33] M. E. Wise, "Tracer dilution curves in cardiology and random walk and lognormal distributions," *Acta Physiologica Pharmacologica Neer-landica*, vol. 14, no. 2, pp. 175–204, 1966.

[34] R. Perera et al., "Real time ultrasound molecular imaging of prostate cancer with PSMA-targeted nanobubbles," *Nanomedicine: Nanotechnology, Biol. Med.*, vol. 28, 2020, Art. no. 102213.

[35] S. Turco et al., "Contrast-enhanced ultrasound quantification: From kinetic modeling to machine learning," *Ultrasound Med. Biol.*, vol. 46, no. 3, pp. 518–543, 2020.

[36] M. Pilgrim and S. Willison, *Dive Into Python 3*, vol. 2. New York, NY, USA: Springer, 2009.

[37] H. W. Lilliefors, "On the Kolmogorov-Smirnov test for normality with mean and variance unknown," *J. Amer. Stat. Assoc.*, vol. 62, no. 318, pp. 399–402, 1967.

[38] M. Mischi, T. A. Kalker, and E. H. Korsten, "Contrast echocardiography for pulmonary blood volume quantification," *IEEE Trans. Ultrasonics, Ferroelect., Freq. Control*, vol. 51, no. 9, pp. 1137–1147, Sep. 2004.

[39] A. Upadhyay and S. V. Dalvi, "Microbubble formulations: Synthesis, stability, modeling and biomedical applications," *Ultrasound Med. Biol.*, vol. 45, no. 2, pp. 301–343, 2019.

[40] J. A. Johnson and T. A. Wilson, "A model for capillary exchange," *Amer. J. Physiol.-Legacy Content*, vol. 210, no. 6, pp. 1299–1303, 1966.

[41] A. R. Pries et al., "The shunt problem: Control of functional shunting in normal and tumour vasculature," *Nature Rev. Cancer*, vol. 10, no. 8, pp. 587–593, 2010.